J. Fluid. Mech. (1982), *vol.* 124, *pp.* 307–334
Printed in Great Britain

Oscillations of an unstable mixing layer impinging upon an edge

By SAMIR ZIADA† AND DONALD ROCKWELL
Department of Mechanical Engineering and Mechanics, Lehigh University, Bethlehem, PA 18015

(Received 25 February 1981 and in revised form 7 June 1982)

The central features of linear and nonlinear disturbance growth in the unstable shear layer, mechanisms of impingement of the resultant vortices on the edge, induced force on the wedge, and upstream influence in the form of induced velocity fluctuations at separation are examined by simultaneous visualization, velocity, and force-measurement techniques.

The nature of the vortex–wedge interaction, and the associated force on the wedge, are directly related to the induced velocity at the upstream separation edge, thereby providing the essential 'feedback' for the self-sustained oscillation. Velocity fluctuations at the upper and lower sides of the separation edge tend to be π out of phase, a condition that is maintained along the outer boundaries of the downstream shear layer. Moreover, the phase between velocity fluctuations at separation and impingement satisfies the relation $2n\pi$, where n is an integer.

The shear layer downstream of the separation edge initially forms an asymmetric wake, which evolves into large-scale vortices, all of which have a circulation appropriate to the high-speed side. The disturbance amplification associated with the high-speed side dominates from the separation edge onwards, precluding development of instabilities associated with the low-speed side.

Regardless of the initial amplitude of the disturbance induced at the separation edge, the same saturation amplitude is attained in the downstream (nonlinear) region of the shear layer, underscoring the fact that variations in force amplitude at the wedge are dominated by the type of vortex–edge interaction mechanism. The sensitivity of this interaction to small offsets between the vortex centre and the leading edge entails that jumps in frequency of oscillation are also associated with jumps in the force amplitude.

1. Introduction

The impingement of separated shear layers on solid boundaries generates a feedback mechanism, which sustains oscillations at selected frequencies from within that band of frequencies at which the shear layer is unstable. Owing to the instability of the shear layer small vorticity perturbations near the separation region are amplified, as they travel downstream, into vortex-like structures. The induced force associated with the impingement of these vortical structures on the solid boundary produces an upstream influence that modulates the sensitive region of the shear layer near separation, in turn giving rise to new vorticity perturbations.

† Present address: Laboratory for vibrations and acoustics, Sulzer Bros, Winterthur, Switzerland.

These oscillations involving a spectrum of configurations such as the jet–edge, jet–orifice, and mixing-layer–edge have been of interest for over a century. Recent reviews by Karamcheti *et al.* (1969), Hussain & Zaman (1978) and Rockwell & Naudascher (1979) describe progress in the study of this class of oscillations, but several aspects await clarification. Of these, the induced force on the impingement edge (or wedge) is central; despite Powell's (1961) recognition that the force is directly associated with the dipole-like behaviour of the disturbances emanating from the domain of the edge and influencing the upstream region of the flow, the detailed nature of the incident unsteady flow–wedge interaction has remained unexplored. The magnitude of the localized loading on the edge and its variation with impingement length, as well as with transverse location of the edge with respect to the incident unsteady shear layer, need to be characterized. When the incident unsteadiness takes the form of coherent vortical structures, the unsteady flow–leading-edge interaction is expected to involve various sorts of deformation of the vortical structure upon its impingement with the edge. Moreover, the possibility that jumps in oscillation frequency are associated with jumps in induced force, as well as with a change in vortex–edge interaction mechanism, should be addressed.

Another aspect to be examined is the degree of upstream influence associated with the force exerted on the wedge. Even for the case of 'pseudosound' (Ffowcs Williams 1969), whereby the distance between shear-layer separation and impingement is much less than an acoustic wavelength, the amplitude of the velocity perturbations induced at the edge of the sensitive region of the shear layer near separation may bear a relation to the magnitude of the force at the edge. Whether this initial fluctuation level at separation typically influences the amplitude of the force exerted on the downstream edge, or simply undergoes nonlinear saturation upstream of the impingement edge, thereby producing essentially identical conditions of unsteadiness (i.e. vortices) approaching the wedge irrespective of the initial fluctuation level, needs to be resolved; that is, the character of the 'amplifier' between separation and impingement as a function of its 'input level' requires clarification.

Also addressed is the problem of finding a phase condition, or the so-called 'phase criterion', which, when incorporated with linear stability theory, permits prediction of the frequency of oscillations. A phase criterion simply specifies the necessary phase shift between the velocity fluctuations at separation and at impingement such that the oscillations are self-sustained. Table 1 is illustrative of contradictory phase criteria found in the literature. Differences in these criteria (shown in table 1) are most probably related to differences in the location (within the shear layer) at which the measurements were taken. Therefore, further consideration of streamwise phase variations of velocity fluctuations measured within the shear layer, as well as at its upper and lower edges, are required to clarify these differences.

With regard to perturbations in the sensitive region of the shear layer (i.e. at the trailing edge), the phasing between fluctuations at the upper and lower sides of the trailing edge is critical; it can be expected to control the disturbance growth immediately downstream of the trailing edge. In turn, the phase between the upper and lower regions of the edge will be influenced by the downstream dynamics of the flow – that is, the upstream influence of downstream unsteadiness must be accounted for.

This investigation focuses on some of these unresolved aspects. Following an examination of the overall nature of system oscillations is an assessment of the evolution of the mean and fluctuating velocities, as well as an evaluation of

Configuration	Investigator(s)	Phase criterion L/λ (n = integer)
Cavity flow	Sarohia (1977)	$n+\frac{1}{2}$
	Rockwell & Schachenmann (1982)	n
	Knisely & Rockwell (1982)	n
Jet–edge	Brown (1937)	$n+\frac{1}{4}$
	Richardson (1931)	n
	Powell (1961)	$n+\frac{1}{4}$
	McCartney & Greber (1973)	$n-\frac{1}{4}$
Jet–wall	Ho & Nosseir (1981)	n
Mixing-layer–edge	Hussain & Zaman (1978)	$n+\frac{1}{2}$

TABLE 1. Previously reported 'phase criteria' for self-sustained oscillations of impinging shear layers

streamwise and transverse phase distributions. Special emphasis is given to the phasing between upper and lower regions of the trailing (separation) edge and to the phase between velocity fluctuations at separation and at impingement. Thereafter, the nature of the induced force is addressed together with its relation to the level of velocity fluctuations at separation and at impingement. The vortex–edge interaction region is then examined in more detail to ascertain whether changes in the amplitude of the wedge force, as the impingement length is varied, are due primarily to differences in the velocity fluctuation level associated with the incident vortex, or to differences in localized vortex–edge interaction mechanisms. The final section deals with the applicability of linear stability theory in describing some of the main features of the system oscillations.

2. Experimental system

2.1. *Mixing-layer–edge model*

During the initial period of designing the test section, attempts were made to generate the mixing layer by placing splitter plates and flow-resistance combinations of different shapes in varying arrangements. The outcome, which proved to be very satisfactory, is shown in figure 1. This arrangement provided an optimum combination of pressure drop along the high- and low-speed sides, which ensured that the leading edge of the divider plate was compatible with the stagnation streamline. In addition, the mildly favourable pressure gradient on both the high- and low-speed sides precluded instability of the boundary layers.

Concerning the wedge assembly, which is shown in figure 1, a 30° included-angle wedge was placed downsteam of the splitter plate. The wedge was attached to a very long Plexiglas plate of equal thickness by means of two side pivots, such that it could rotate freely and with minimum friction. This arrangement eliminated any upstream influence from the wake of the wedge, thereby simulating the impingement of a vortical structure on the leading edge of a semi-infinite plate. The wedge–plate assembly was suspended by three brass supports from a carrier that was placed on the top of the sidewalls of the test section. Since the small dimensions of the wedge provided insufficient space to fit pressure transducer(s), a highly sensitive strain-gauge system was developed to measure the total (integrated) fluctuating force on the wedge (Ziada 1981). As shown in figure 1, the wedge was held in the mid-position by two

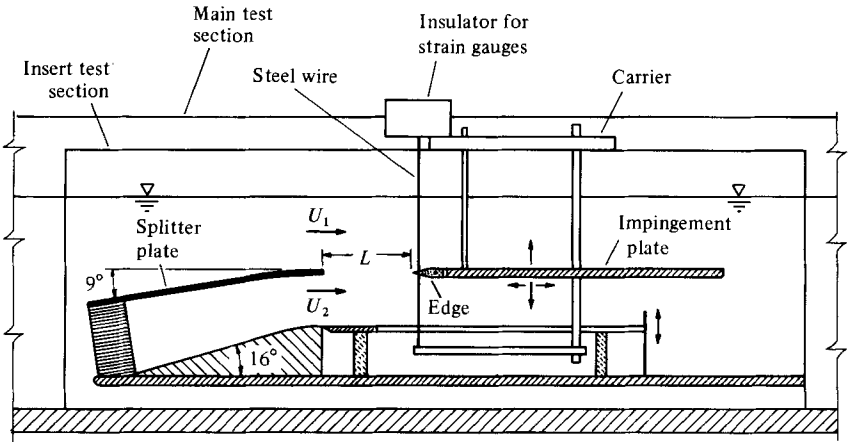

FIGURE 1. Overall view of test section.

stainless-steel vertical wires under tension. The bottom end of the wire was tightened to a brass rod connected to an extension from the downsteam support of the wedge assembly, while the upper end was connected to the strain-gauge system, which was mounted on top of the carrier. Tests to determine the natural frequency of the wedge system revealed it to be 14 Hz in water and 35 Hz in air, giving an added-mass factor of 5·25. The frequencies of interest were about 3·5 Hz for the fundamental and about 7 Hz for the first harmonic. Amplitude and phase distortions of the force signal at the frequency of the fundamental mode of interest here were therefore estimated to be 5 % and 1·9° respectively.

In order to bypass the sidewall and floor boundary layers generated upstream of the test section, the flow divider and the wedge were assembled inside a secondary test section, which was inserted, as shown in figure 1, into the main test section of a free-surface, closed-circuit water channel. The main test section, 30·5 cm wide by 45·7 cm deep, as well as the insert test section, 24 cm wide, were of Plexiglas to facilitate flow-visualization studies. Extensive studies were carried out to ascertain that, for the range of parameters considered in this investigation, the free surface did not influence the basic nature of the oscillation. Instability fluctuations induced in the shear layer were found to drop off exponentially as the free stream was approached, in accordance with linear stability theory. In the free stream, organized fluctuations were undetectable, even when the lock-in amplifier was used to enhance the detection capability.

2.2. *Instrumentation*

Extensive velocity measurements were taken by means of DISA hot-film probes (55T11 and 55R14) using a DISA 55D01 anemometer in conjunction with a DISA 55M25 linearizer. Velocity and force signals were filtered and amplified by Krohn–Hite Model 3700 bandpass filters and class A variable-gain amplifiers. The nominal filtering frequencies were 0·2 Hz and 20 Hz for all measurements, whereas the typical frequencies of interest were in the range 2·9–3·7 Hz. Spectral analysis of the velocity and force signals was performed with the aid of a PDP-8 minicomputer. Phase measurements were carried out by means of an Ortec phase-lock wave analyser with low frequency, high-stability and high-resolution options. The velocity signal was fed to the signal channel, whereas the force signal was fed to the reference channel.

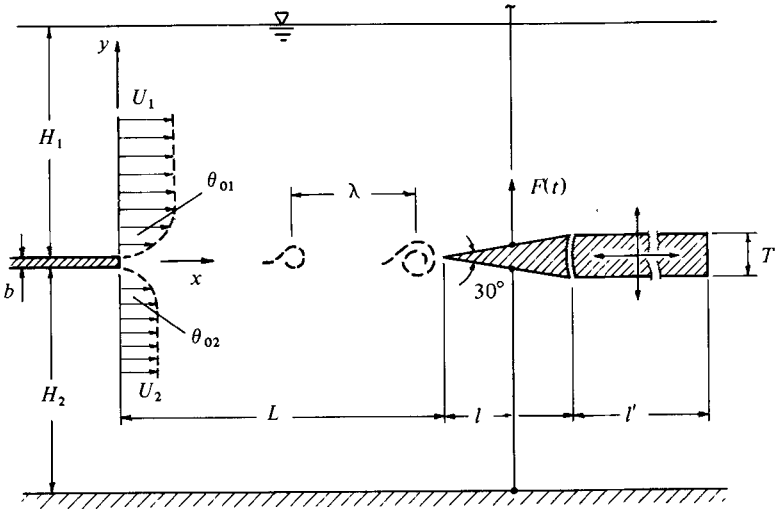

FIGURE 2. Mixing-layer–wedge arrangement.

2.3. *Flow-visualization techniques*

Visualization was carried out using the hydrogen-bubble and dye-injection methods. For the hydrogen-bubble method, a vertical platinum wire (0·002 in.) was used in a manner that permitted its positioning at any streamwise location, whereas, in the dye-injection method, food colour dye was laid on the top surface of the splitter plate. The lighting arrangement, particularly critical for effective bubble contrast, is described in detail in Ziada & Rockwell (1982*a*). The time-dependent evolution of the visualized vortex–wedge interaction and the instantaneous force fluctuation (displayed on a storage oscilloscope) were recorded simultaneously on a split-screen Instar television system having vertical and horizontal sweep frequencies of 120 Hz and 25·2 kHz, a resolution of 250 lines, and a framing rate of 120 frames per second. Photos shown herein were obtained by taking 4 in. × 5 in. Polaroids of the image on the video screen.

2.4. *Flow parameters*

The relevant dimensions of the mixing-layer–edge arrangement are shown in figure 2. All measurements were taken at a flow speed of 18·35 cm/s at the high-speed side (U_1) and velocity ratio $U_1/U_2 = 2{\cdot}85 \pm 0{\cdot}05$. These conditions provided extremely well-defined vortices in the downstream mixing layer with laminar boundary layers at separation having momentum thicknesses $\theta_{01} = 0{\cdot}62$ mm and $\theta_{02} = 0{\cdot}68$ mm, θ_0 being their sum. The corresponding Reynolds number was

$$Re(\Delta U, \theta_0) = (U_1 - U_2)\theta_0/\nu = 157 \quad \text{or} \quad Re(U_1, \theta_0) = U_1\theta_0/\nu = 239.$$

Other relevant parameters (see figure 2) had the following values: $H_1/\theta_{01} = 126$; $H_2/\theta_{02} = 115$; $b/\theta_0 = 3$; $l'/\theta_0 = 350$, $T/\theta_0 = 15$; $15 \leqslant L/\theta_0 \leqslant 150$. At this speed, the streamwise fluctuation velocity in the free stream was about 0·06%. Extensive spanwise flow visualization showed that the flow field was essentially two-dimensional along the entire length from separation to impingement for all impingement lengths examined.

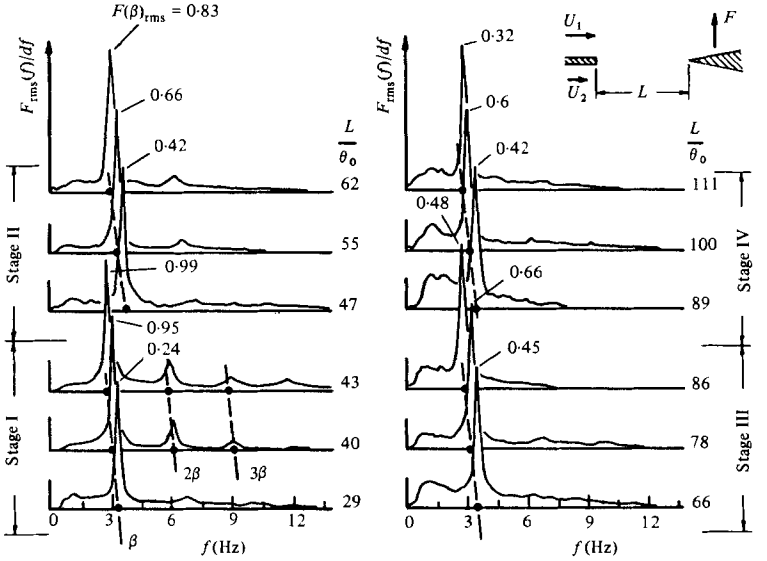

FIGURE 3. Typical spectra of induced force $F_{rms}(f)/df$ versus f on wedge for different impingement length L/θ_0.

3. Overall nature of oscillations

3.1. *Frequency and amplitude of induced force*

The overall nature of system oscillations typical of self-sustained oscillations of impinging shear layers is characterized by the existence of so-called 'stages' of operation. During each stage, the fundamental frequency β decreases continuously with increases in impingement length L. At a certain length a frequency jump to a higher frequency occurs, marking the beginning of a new stage. Thereafter, further increases in L result in a gradual decrease in β until the next frequency jump. These characteristics were quantified in this investigation by measuring the induced force on the edge. Representative frequency spectra of the induced force are depicted in figure 3. The relative magnitude of the spectral peak, as well as the dimensionless impingement length, are shown on each spectrum. Each stage of the observed four stages of oscillation is illustrated by three frequency spectra: the first spectrum is at the beginning of each stage (i.e. just after the frequency jump from the previous stage); the second spectrum is roughly at the middle of the stage; and the third spectrum is at the end of the stage.

For impingement lengths shorter than those corresponding to figure 3 ($L/\theta_0 \leqslant 29$) no oscillations were observed. Flow-visualization studies revealed that the separated shear layers from the top and bottom of the trailing edge experienced reattachment at the leading edge of the wedge without showing any sign of oscillatory behaviour.

The spectra shown in figure 3 indicate that the system oscillations are of a highly organized nature: most of the fluctuation energy is concentrated at the fundamental frequency $\beta = f\theta_m/U_1$, where θ_m is the characteristic momentum thickness. As will be shown by means of flow visualization, this frequency corresponds to the frequency of vortex formation upstream of the edge. Also, a weak energy concentration can be seen at the frequencies of the higher harmonics (2β, 3β), most evident in the first two stages; this presence of the higher harmonic components is due to the nonlinear nature of the shear-layer evolution (Ziada & Rockwell 1982*b*).

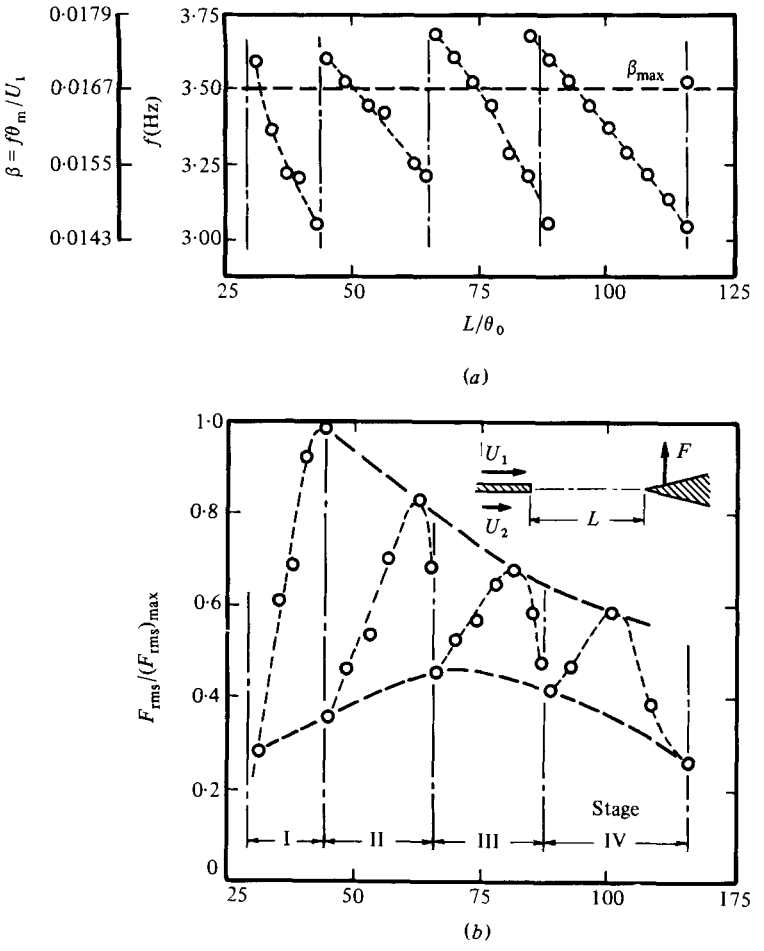

FIGURE 4. Amplitude F_{rms} and frequency f of the dominant spectral peak of force fluctuations as functions of impingement length L/θ_0: (*a*) dimensionless frequency $\beta = f\theta_m/U_1$ versus L/θ_0; (*b*) normalized force $F_{rms}/(F_{rms})_{max}$ versus L/θ_0.

The magnitudes and frequencies of the dominant spectral peaks from figure 3 are plotted against impingement length in figure 4. Distinct stages of operation, separated by frequency jumps, can be discerned – successively higher stage numbers relate to longer impingement lengths. Each frequency jump is associated with a sudden drop in the force amplitude, the magnitude of this drop decreasing at larger values of impingement length. The maximum force amplitude in each stage is also seen to decrease with longer impingement lengths.

For the oscillations to be self-sustained, two compatibility conditions have to be satisfied. First, a constant phase shift has to be maintained between the velocity fluctuations at separation and at impingement. Secondly, the frequency of oscillation has to be in the neighbourhood of the frequency β_{max} at which the shear layer is most unstable. As the impingement length is gradually increased, satisfaction of the phase condition requires a corresponding increase in the wavelength of the instability wave. Thus, according to the stability theory (Michalke 1965) the frequency of oscillation gradually decreases. The result is that the frequency β drifts away from β_{max}, as indicated in figure 4 (*a*). At a certain length of impingement, a higher frequency, which

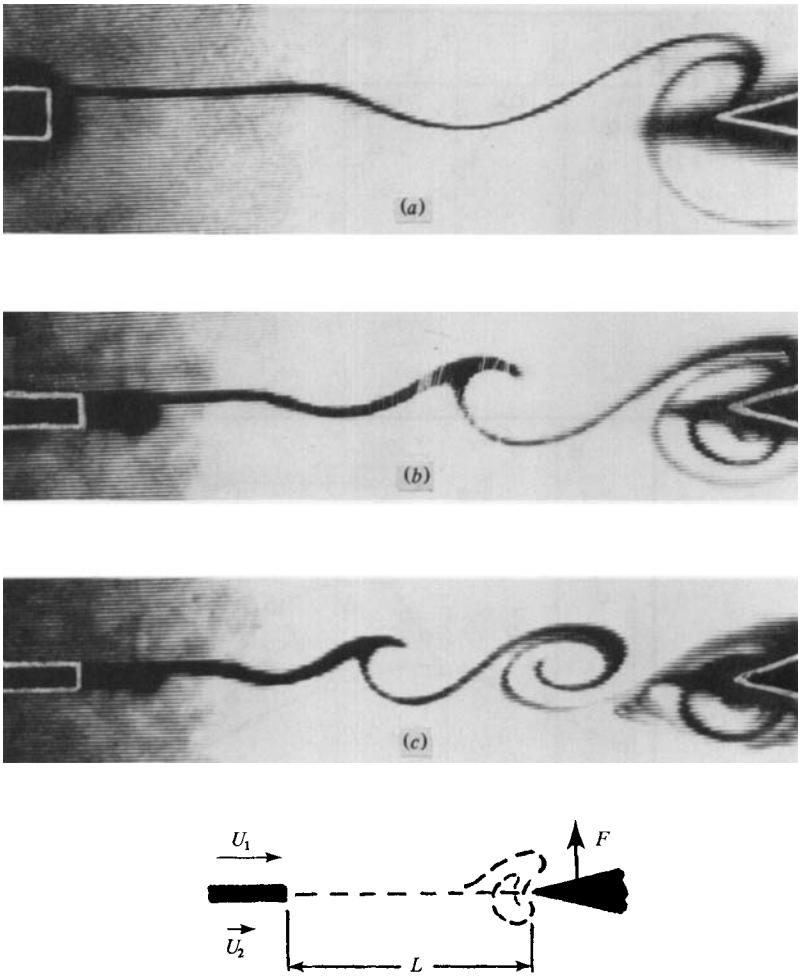

FIGURE 5. Visualization of mixing-layer–wedge interaction patterns for different impingement lengths corresponding to oscillations in stages I–III: (*a*) $L/\theta_0 = 42$, stage I; (*b*) $L/\theta_0 = 62$, stage II; (*c*) $L/\theta_0 = 81$, stage III. $Re = \Delta U\theta_0/\nu = 157$.

is closer to β_{max}, can satisfy the phase condition through the addition, as it were, of a single wavelength to the instability wave between separation and impingement, causing a frequency jump, as shown in figure 4(*a*). This explains the physical mechanism through which the frequency of oscillation adjust itself to variation in the impingement length. As for the relationship between the force amplitude and the impingement length depicted in figure 4(*b*), the physical mechanism involved is by no means obvious. This aspect is addressed subsequently.

3.2. *Flow visualization of the system oscillations*

Owing to the finite thickness of the blunt trailing edge at separation, the free shear flow first starts as an asymmetric wake and then gradually evolves into a mixing layer. This might lead one to think that the two separating shear layers independently roll up into an asymmetric vortex street. However, this was not the case, as can be seen

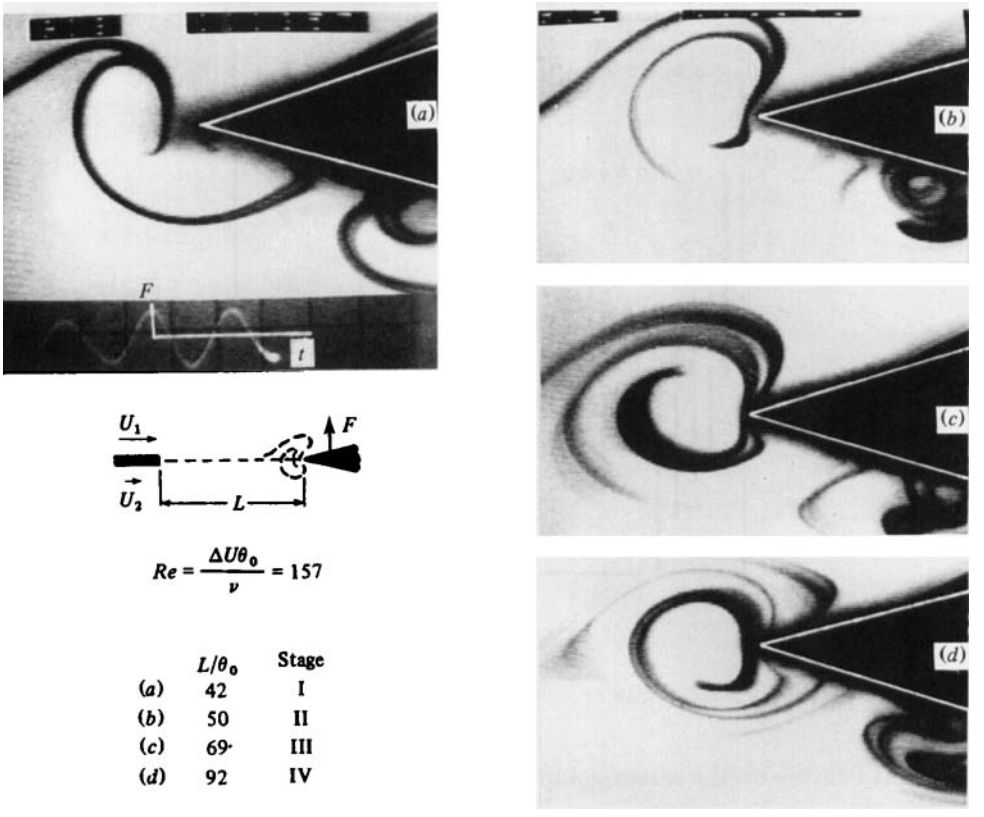

	L/θ_0	Stage
(*a*)	42	I
(*b*)	50	II
(*c*)	69	III
(*d*)	92	IV

FIGURE 6. Visualization of vortex–wedge interaction patterns for different impingement lengths corresponding to oscillations in stages I–IV.

from the flow-visualization pictures in figure 5. The separated shear flow was found to evolve into a single row of well-defined vortical structures having circulation appropriate to the high-speed side owing to the sufficiently thick boundary layers at the trailing-edge. Extensive flow-visualization studies of the trailing-edge flow region, using dye and hydrogen bubbles, revealed the complete absence of vortex formation in the shear layer on the low-speed side.

Scrutiny of photos (*a*)–(*c*) of figure 5 reveals that each successive stage contains one more vortical structure between separation and impingement than the previous stage; for instance, photo (*c*), relating to stage III, reveals one more vortex than photo (*b*), relating to stage II. This illustrates the increase in the number of wavelengths of the instability wave between separation and impingement entailed in frequency jumps to higher stages.

The close-up visualization photos of figure 6, taken at the instant when the induced force on the wedge attained its maximum negative value, show that the incident vortex becomes more 'mature', i.e. the roll-up process becomes more developed, at larger values of impingement length. Moreover, as can be seen by examining photos (*b*)–(*d*), the centre of the vortex is lower, relative to the leading edge, at longer impingement lengths, agreeing well with the trend of the theoretical trajectories of vortex impingement upon the leading edge of a semi-infinite plate (Rogler 1974). As will be discussed, the variation of the transverse offset between the centre of the incident vortex and the leading edge as the impingement length is varied has an

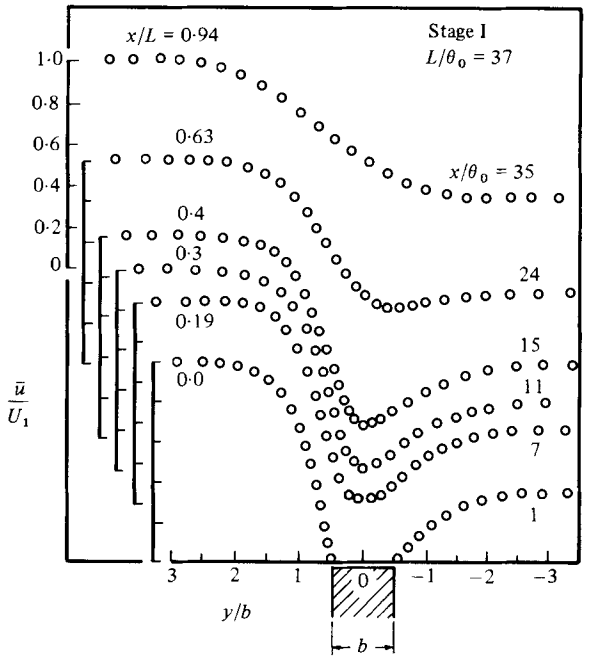

FIGURE 7. Streamwise evolution of mean-velocity distribution $\bar{u}(y)$.

important bearing on the relationship between the force amplitude and the impingement length.

4. Mean and fluctuating velocity field

For carrying out the velocity measurements, an impingement length $L/\theta_0 = 37$ was selected as optimal. At that length (corresponding to stage I operation) the induced force on the edge is relatively high, indicating a strong mixing-layer–edge interaction, away from the occurrence of a frequency jump. Important for our consideration is the fact that initial momentum thicknesses (corresponding to laminar boundary layers) on the high- and low-speed sides of the splitter plate are nearly equal ($\theta_{01} = 0{\cdot}062$ cm and $\theta_{02} = 0{\cdot}068$ cm). Consequently, differences in dimensionless frequency parameter $f\theta_0/U$ will be due only to the difference between U_1 and U_2 at a given frequency of oscillation.

Figure 7 depicts the streamwise evolution of the mean-velocity profile. Shortly after separation, the separated shear layers from the top and bottom sides of the splitter plate merge and form an asymmetric wake profile, which continues to change in shape until a mixing-layer profile is achieved.

At each streamwise station x/L, spectral analysis of the streamwise velocity fluctuation $\tilde{u}$ was performed at different transverse (y) locations. The spectral peaks at the fundamental frequency β are plotted in figure 8, giving the streamwise evolution of the distributions of the streamwise velocity fluctuations (i.e. distributions of $\tilde{u}(\beta)_{\mathrm{rms}}$). As shown by Ziada (1981), the shape of these distributions at large x/θ_0 is well approximated by the variable-vorticity-concentration model of Stuart (1967).

The streamwise evolution of the two maxima of the fluctuating velocity distrib-

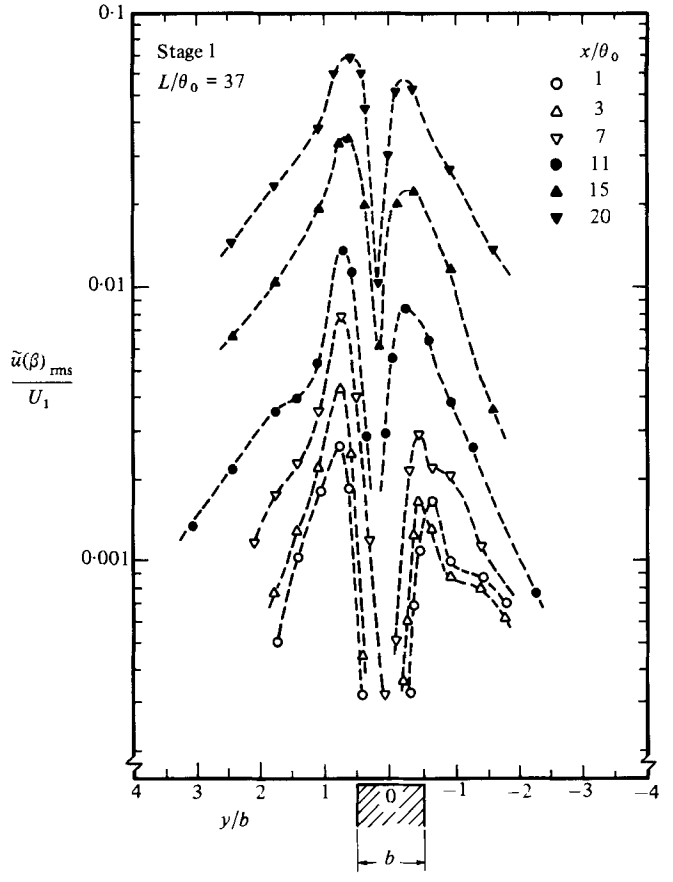

FIGURE 8. Evolution of distribution of normalized fluctuation velocity $\tilde{u}(\beta)_{\rm rms}/U_1$ in streamwise direction.

utions is highlighted in figure 9. Open symbols represent the streamwise growth of the maximum r.m.s. fluctuation velocity ($\tilde{u}(\beta)_{\rm M1}$) at the high-speed side, whereas solid data points symbolize that ($\tilde{u}(\beta)_{\rm M2}$) at the low-speed side. In the immediate vicinity of separation, $\tilde{u}(\beta)_{\rm M1}$ exhibits an exponential growth followed by a region of nonlinear amplitude saturation, then decays as it approaches the wedge-flow region. For the low-speed side, $\tilde{u}(\beta)_{\rm M2}$ remains virtually constant over a distance of $9\theta_{01}$, after which it starts growing rapidly with a growth rate even higher than that for $\tilde{u}(\beta)_{\rm M1}$; in fact it appears to be driven by the dominant fluctuation on the high-speed side. This drastic difference in growth rates for the near-field region can be explained using linear stability theory (Michalke 1965). At the streamwise location corresponding to the centre of the linear-growth region of $\tilde{u}(\beta)_{\rm M1}$ (figure 9) the momentum thicknesses of the shear layers at the high- and the low-speed sides ($\theta_{\rm m1}$ and $\theta_{\rm m2}$ respectively) can be used to calculate the dimensionless frequencies β_1 and β_2 ($\beta_1 = f\theta_{\rm m1}/U_1 = 0{\cdot}0155$ and $\beta_2 = f\theta_{\rm m2}/U_2 = 0{\cdot}045$). According to the linear spatial stability theory, β_1 approximates that frequency at which the shear layer is most unstable ($\beta_{\rm max} = 0{\cdot}0165$), whereas β_2 is found to lie outside the band of frequencies at which the shear layer is unstable ($0 < \beta < 0{\cdot}04$). In other words, the high-speed-side shear layer is highly unstable at the frequency of the mixing-layer–edge operation, whereas

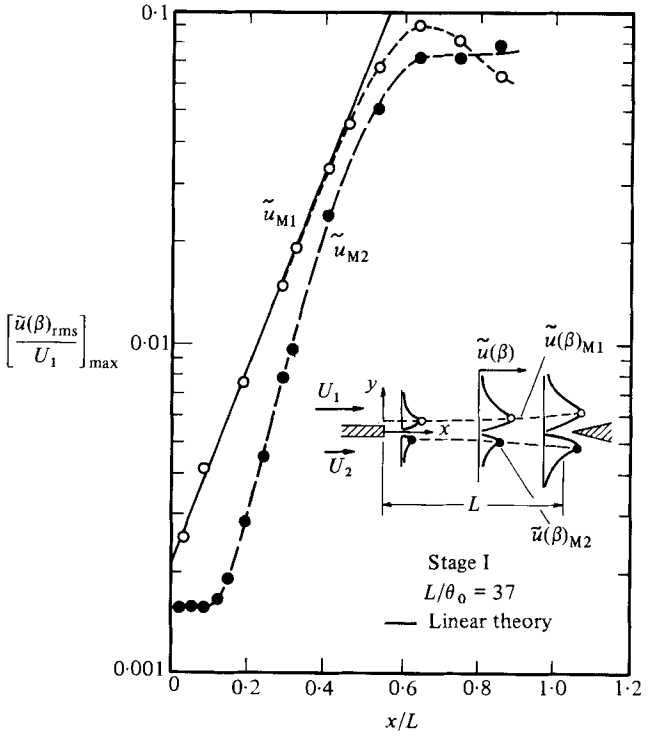

FIGURE 9. Streamwise growth of fluctuation velocity maxima $\tilde{u}(\beta)_{M1}$ and $\tilde{u}(\beta)_{M2}$.

disturbances at this frequency do not, at least initially, experience amplification in the shear layer on the low-speed side. As shown in figure 9, there is excellent agreement with linear stability theory.

Further downstream ($x/L = 0{\cdot}35$), the shear layers merge into one another. In that region, stability analysis carried out for each layer separately is unjustified. Only stability analysis of local velocity profiles is appropriate. Miksad (1972) performed such an analysis for an asymmetric wake-type flow. Two types of instability arose. 'Type I [no relation to our stage I!] instability' was associated with the inflection point at the high-speed side, and 'type II instability' with that on the low-speed side; the type I instability was found to have *much higher growth rates* and occur over *a much wider range* of frequencies than the growth rates and frequency range associated with type II instability. Miksad therefore speculates that the high-speed-side shear layer dominates, a contention supported by the complete absence of type II instability in his experiment. These findings are in agreement with the present observation, namely that instability of the high-speed-side shear layer dominates the oscillation characteristics.

5. Phase variations

In the following, the nature of phase distributions across the shear layer† is discussed, especially with regard to the region immediately downstream of separation. Then, phase variations in the streamwise direction† are examined and compared with those of table 1.

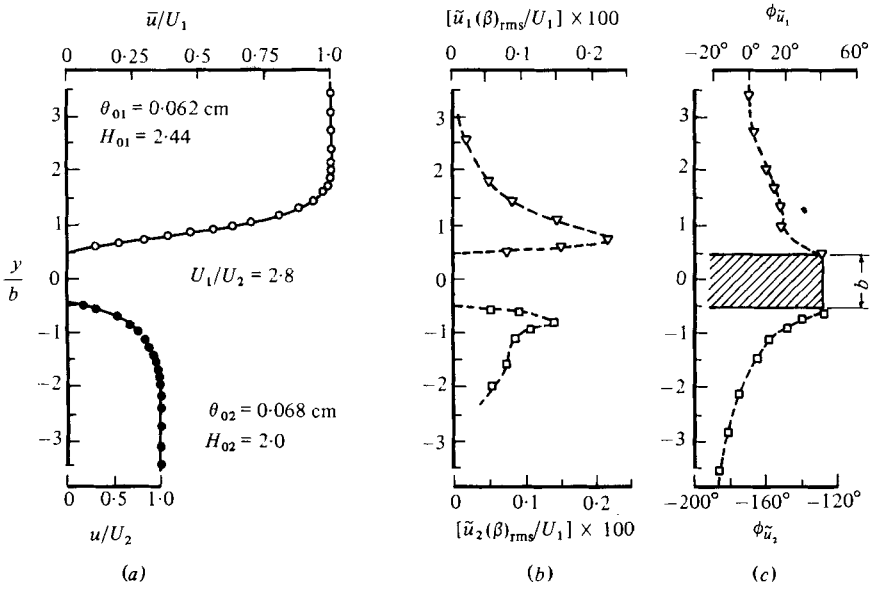

FIGURE 10. Initial conditions at the trailing edge of the splitter plate ($x = 0$): (a) mean-velocity profile $\bar{u}(y)$; (b) transverse distribution of fluctuation velocity $\tilde{u}(\beta)_{\rm rms}$; ($c$) transverse distribution of fluctuation velocity phase $\phi_{\tilde{u}(\beta)}$. $L/\theta_0 = 37$, corresponding to stage I oscillation.

5.1. *Transverse phase variations at trailing edge and in downstream shear layer*

Figure 10 shows details of the initial conditions at separation (for $L/\theta_0 = 37$, corresponding to an oscillation in stage I), including mean-velocity profiles, distributions of $\tilde{u}(\beta)_{\rm rms}$, and phase distributions of $\tilde{u}(\beta)$. Phase data are referenced to the phase of $\tilde{u}(\beta)$ in the free stream at the high-speed side of the flow. The phase relationship between the velocity fluctuations on both sides of the splitter plate, extracted from the data of figure 10(c), is presented in figure 11(a). At separation, the phase distribution of $\tilde{u}(\beta)$ at the high-speed side is approximately 180° out of phase with that at the low-speed side. In other words, *at separation, the velocity fluctuation at a point on the high-speed side is virtually π out of phase with that at its mirror image on the low-speed side*. This result, which persists through stage II operation, as can be seen in figure 11(b), would appear to be independent of the laminar-boundary-layer characteristics. The maximum deviation from this phase relationship between the velocity fluctuation on both sides of the splitter plate is about 8 % and occurs for small values of $|y|$, i.e. inside the boundary layer. For large values of $|y|$, outside the boundary layer, the deviation reduces to about 3 %.

The overall phase difference across the boundary layer is in the range of 30°–50°. This is very similar to the theoretical and experimental findings of overall phase difference across forced laminar boundary layers (Hill & Stenning 1960). The relative insensitivity of the overall phase difference across the boundary layer to changes in either shape factor or frequency of oscillation in this experiment is also similar to that found for forced laminar boundary layers. This would seem to suggest similarities between the two cases; however, there is a major difference. Whereas in the case of

† In the text that follows, distributions of phase of the velocity fluctuation across the shear layer (y-direction) will be denoted as 'transverse phase variations', while those in the streamwise (x-direction) will be termed 'streamwise phase variations'.

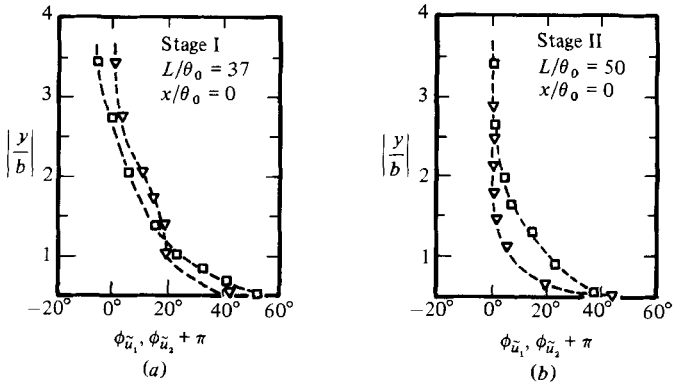

FIGURE 11. Phase relation between fluctuation velocity on either side of the trailing edge of the splitter plate at $x = 0$.

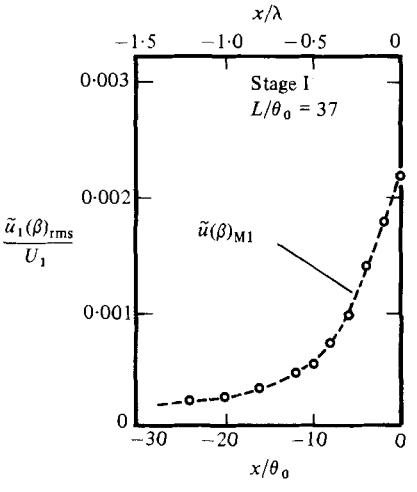

FIGURE 12. Maximum fluctuation velocity $\tilde{u}(\beta)_{M1}$ as a function of streamwise location x/θ_0 upstream of the trailing edge of the splitter plate.

an externally forced (laminar) boundary layer the amplitude of the free-stream fluctuation is virtually constant, in this experiment, the amplitude of the maximum velocity fluctuation $\tilde{u}(\beta)_{M1}$ decays exponentially upstream of separation (figure 12). Consequently, the transverse scale (dimensionless y) of the distributions of $\tilde{u}(\beta)_{rms}$ and $\phi_{\tilde{u}}$ was found to be about an order of magnitude smaller than the corresponding scale of forced boundary layer (Hill & Stenning 1960). Clearly figures 10 and 11 show the *upstream imprint of the downstream phasing of unsteady events across the shear layer; that is, the remarkably consistent phase difference of* $\sim \pi$ *across the trailing edge is driven by the downstream dynamics.* That there must be compatibility between the trailing-edge dynamics and the downstream evolution is suggested by figure 13; the phase difference between oscillations at the upper and lower sides of the shear layer is maintained at a constant value of about π along the streamwise extent of the mixing layer.

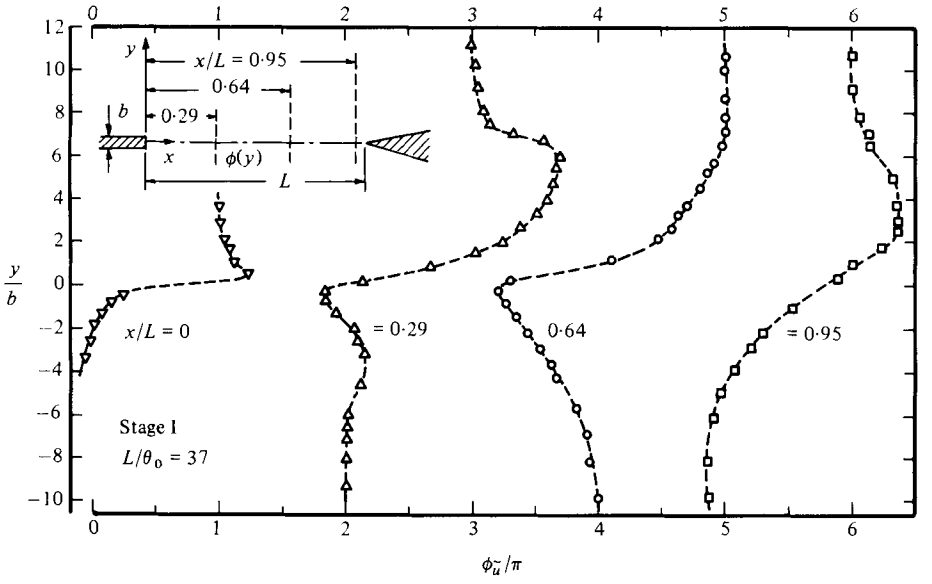

FIGURE 13. Streamwise evolution of the phase distribution of the fluctuation velocity $\phi_{\tilde{u}}(y)$.

5.2. *Streamwise phase variations*

The large variations in the transverse phase distribution shown in figure 13 clearly indicate that a proper criterion for streamwise phase measurements is crucial in the search for a universal phase law for self-sustained oscillations. The criteria to be considered herein are:

(i) phase variations measured along a y = constant line ($y/b = 0, y/b = \frac{1}{2}, y/b = -\frac{1}{2}$), designated $\phi(0)$, $\phi(\frac{1}{2})$, $\phi(-\frac{1}{2})$ respectively;

(ii) phase variations measured along the loci of y-locations at which the r.m.s. velocity fluctuation is at a maximum ($\tilde{u}(\beta)_{M1}$ and $\tilde{u}(\beta)_{M2}$ defined in figure 9), designated $\phi(\tilde{u}_{M1})$ and $\phi(\tilde{u}_{M2})$;

(iii) streamwise phase distributions measured at the upper and lower edges of the shear layer ($\bar{u}/U_1 = 0{\cdot}95$ and $\bar{u}/U_2 = 0{\cdot}95$), designated $\phi(0{\cdot}95)$ and $\phi(-0{\cdot}95)$.

The resultant phase distributions are shown in figure 14. It should be noted that, immediately downstream of separation (small x/θ_0), the velocity signal was very well defined except along the line $y = 0$. Extrapolation to $x = 0$ was necessary in this region.

Only the phase distributions measured at the upper and the lower edges of the shear layer appear to have an obvious significance; they exhibit overall phase shifts between separation and impingement of about $2n\pi$, and linear variations of phase in the streamwise direction. This is hardly surprising, since phase measurements within the shear layer encounter the problems of not only the high transverse phase gradients and phase distortions near separation and impingement, but also the increased contributions from the transverse velocity fluctuations $\tilde{v}$ in the regions where the mean velocity is low. Measurements at the edge of the shear layer are essentially uninfluenced by these effects.

Phase distributions measured at the upper *and* lower edges of the shear layer in stage II were found to exhibit behaviour similar to that in stage I, further suggesting that only phase measurements at the edge of the shear layer would give a unique and generalized phase criterion for self-sustaining oscillations. The phase data plotted

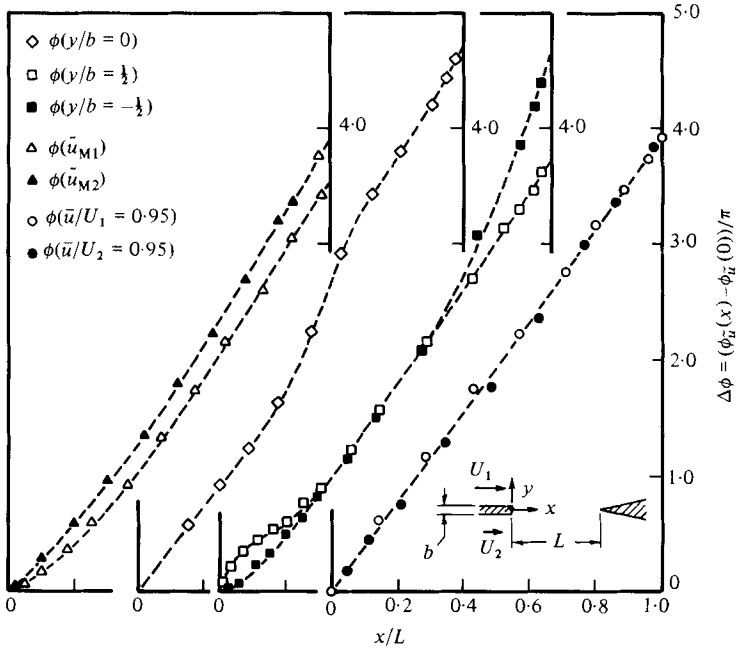

FIGURE 14. Comparison of streamwise distributions of fluctuation velocity phase $\phi_{\tilde{u}}(x)$ resulting from employing different criteria for phase measurement. $L/\theta_0 = 42$, corresponding to stage I oscillations.

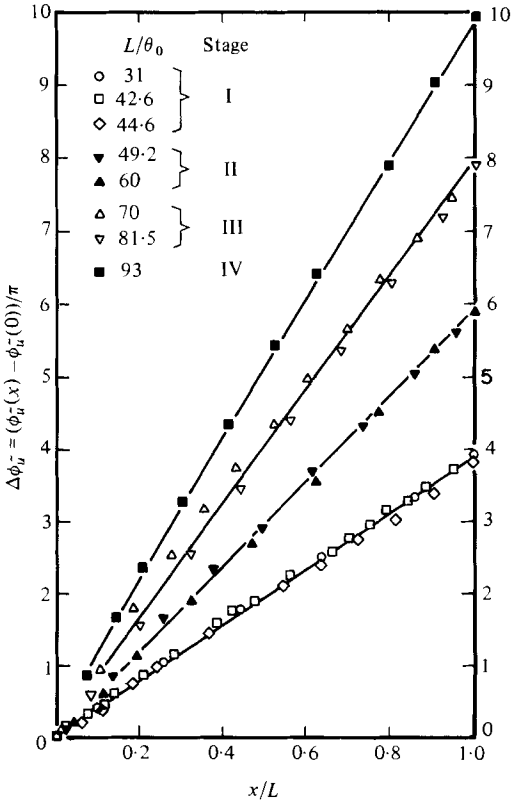

FIGURE 15. Streamwise variation of fluctuation velocity phase $\phi_{\tilde{u}}(x)$ at upper edge of mixing layer ($\bar{u}/U_1 = 0{\cdot}95$) for oscillations in stages I–IV.

in figure 15 illustrate that this is indeed the case. These phase data are measured at the upper edge of the shear layer for several impingement lengths, through each of the four stages of operation. From these phase data it can be concluded that:

(i) an appropriate overall streamwise phase criterion for self-sustaining oscillations is

$$\phi_{\tilde{u}}(x = L) - \phi_{\tilde{u}}(x = 0) \approx 2\pi n, \tag{1}$$

where n is an integer;

(ii) the phase of the velocity fluctuation $\tilde{u}$ along the edge of the shear layer varies linearly in the streamwise direction. Consequently, the disturbance phase speed c and wavelength λ are virtually constant along the entire region from separation to impingement.

These findings lead to the result $L/\lambda = n$. In other words, the organized activity in the shear layer, characterized by growth and saturation of the disturbance, has a wavelength, or multiple of wavelengths, equal to the impingement length.

From table 1 it can be seen that the result $L/\lambda = n$ agrees with the findings of Rockwell & Schachenmann (1982), Knisely & Rockwell (1982), and Ho & Nosseir (1981), all of whose results are taken outside the shear layer. The term $-\frac{1}{4}$ in McCartney & Greber's (1973) theoretical result should, as they themselves note, tend to zero had they not for simplicity's sake ignored minor terms in their analysis. Sarohia's (1977) and Hussain & Zaman's (1978) measurements were both taken inside the shear layer, Sarohia's at the mouth of the cavity, Hussain & Zaman's being extrapolated from measurements of maximum phase over an axial distance less than the impingement length. Thus, in view of the results shown in figure 14, the disagreement is not surprising. To be sure, measurements within the shear layer are important as well; their relation to those at the edge of the shear layer deserves further attention.

6. Nature of the induced force

6.1. *Effect of unsteady velocity amplitude upstream of impingement*

Measurements of the streamwise evolution of the velocity fluctuations $\tilde{u}(\beta)_{\rm rms}$ can provide insight into the extent that $\tilde{u}$ near separation, $\tilde{u}$ near impingement, induced force F, and impingement length L are interrelated. Figure 16 depicts detailed measurements, taken in stage II, showing streamwise evolutions of *maximum* $\tilde{u}(\beta)_{\rm rms}$ (i.e. $\tilde{u}(\beta)_{\rm M1}$), $\tilde{u}(\beta)_{\rm M1}$ values at separation versus L/θ_0, and the variation of $F_{\rm rms}$ with L/θ_0. For purposes of illustration, the separation point ($x = 0$) in figure 16 is displaced to the left by an amount equal to the increase in the impingement length. This facilitates a clear comparison between the approaching $\tilde{u}(\beta)_{\rm M1}$ at similar distances upstream of the edge. As shown in the inset of figure 16, three different values of impingement length are considered: first, that length at which the induced force is at a minimum during stage II (case (*b*)); secondly, that corresponding to the middle of stage II where the force has an intermediate value (case (*c*)); and thirdly, that at which the maximum force during stage II is induced (case (*d*)). The increase in amplitude of the streamwise velocity fluctuation at separation $\{u_{\rm rms}(\beta)\}_{x=0}$ with increase in force induced at the wedge establishes the link between events at impingement and those at separation: the strength of the dipole-like field at the wedge is directly manifested in the induced velocity field at separation.

The most striking result of figure 16 is that, although the amplitude of the induced force exhibits a strong dependence on the impingement length, the r.m.s. amplitudes of the velocity fluctuations $\tilde{u}(\beta)_{\rm M1}$ in the region upstream of the wedge are nearly

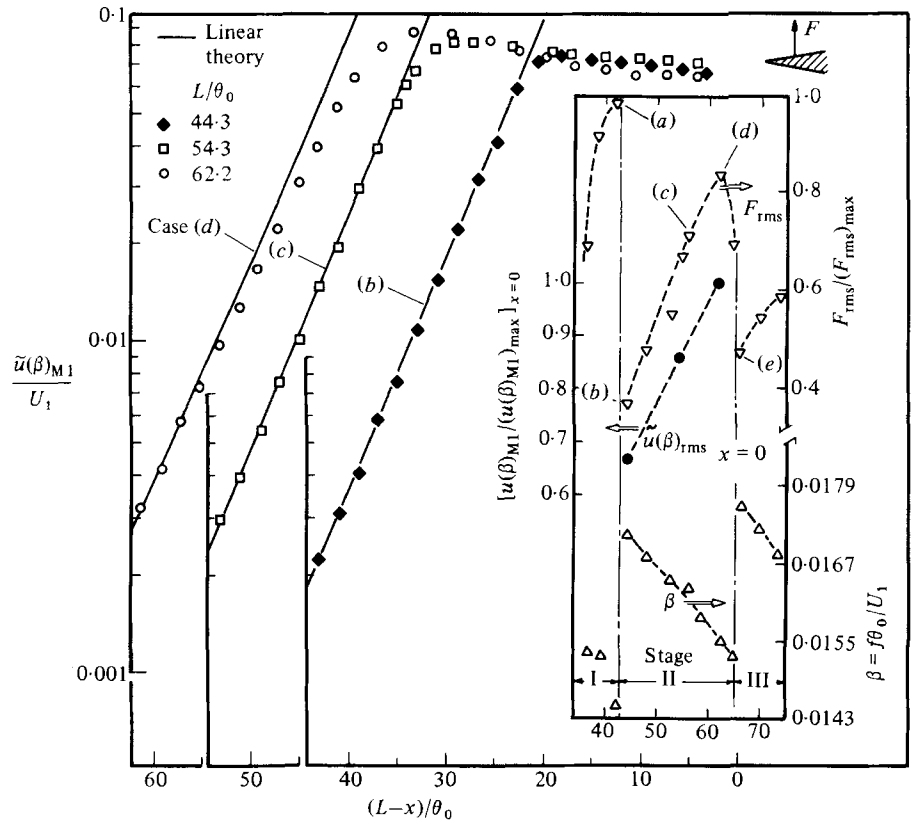

FIGURE 16. Streamwise evolution of maximum fluctuation velocity $\tilde{u}(\beta)_{M1}$ for three impingement lengths corresponding to stage II oscillations. Shown in the inset are details of stage II oscillations: variation of force F_{rms}; variation of fluctuation velocity at separation $(\tilde{u}(\beta)_{M1})_{x=0}$; and variation of frequency β of oscillation with impingement length.

the same for all three cases (*b*), (*c*), (*d*). Despite the different initial values of $\tilde{u}(\beta)_{M1}$ at separation, $\{\tilde{u}(\beta)_{M1}\}_{x=0}$, the occurrence of amplitude saturation of the disturbances at locations upstream of the leading edge of the wedge makes $\tilde{u}(\beta)_{M1}$ values nearly equal. *Consequently, variations of the r.m.s. amplitudes of the incident velocity fluctuations are not the source of the large (relative) variations in magnitude of the induced force.*

These observations strongly suggest that the local vortex–wedge interaction is linked to the variation of induced force amplitude with impingement length. In examining this aspect, consideration must be given to the possibility of different vortex–leading-edge interaction mechanisms as the impingement length is varied. This effect of variation in interaction mechanism is considered in §6.2, which first addresses the sensitivity of the interaction mechanism to very small changes in transverse position of the centre of the vortex to the leading edge of the wedge at a constant value of impingement length; then the interaction mechanisms at zero offset for varying impingement lengths are studied.

6.2. *Effect of vortex–edge interaction pattern*

Selected flow-visualization photos showing the nature of the vortex–wedge interaction mechanism (using hydrogen bubbles) are reproduced in figure 17. The impingement length for the three photos is the same ($L/\theta_0 = 58$) whereas the values of ϵ/θ_R are

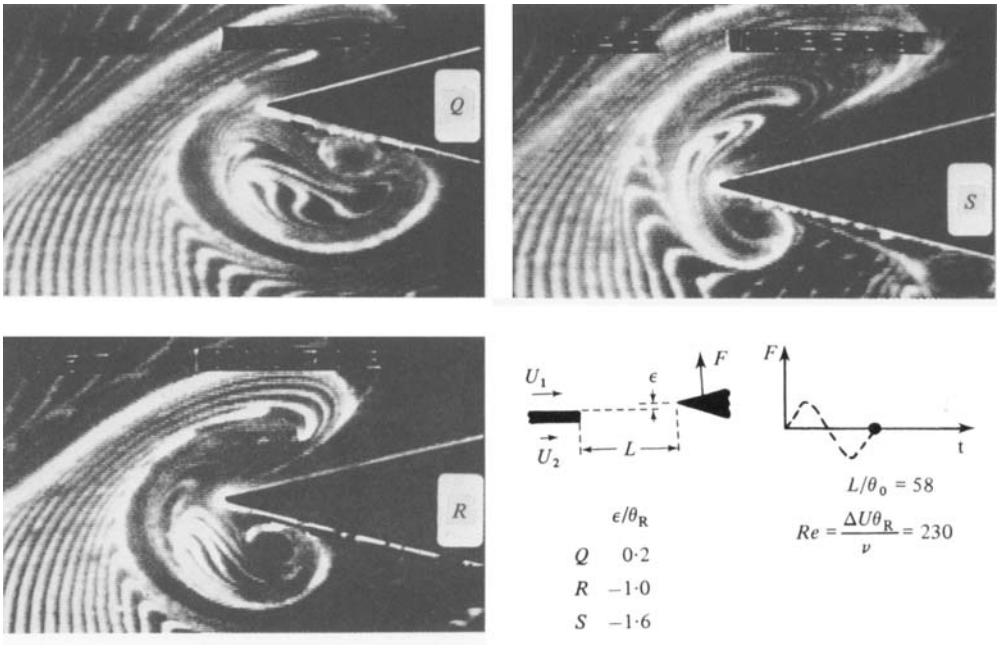

FIGURE 17. Visualization of effect of transverse location ϵ/θ_R of wedge at constant impingement length ($L/\theta_0 = 58$) on vortex–wedge interaction patterns.

different; ϵ represents the transverse or geometric offset of the leading edge of the wedge from the elevation of the upper surface of the splitter plate, and θ_R is the momentum thickness just upstream of impingement ($\theta_R/\theta_0 = 1{\cdot}32$). All photos represent the same instant of the force cycle, i.e. zero force, as illustrated.

The first photo of figure 17 (photo Q; $\epsilon/\theta_R = 0{\cdot}2$) indicates the passage of the larger part of the severed vortex under the wedge; the second photo (photo R; $\epsilon/\theta_R = -1{\cdot}0$) portrays the vortex whilst in the process of splitting into halves above and below the wedge; and the third photo (photo S; $\epsilon/\theta_R = -1{\cdot}6$) illustrates the escape of the larger part of the incident vortex above the wedge. A secondary vortex forms, with opposite vorticity to that of the incident vortex, at the lower side of the wedge. This secondary and opposite vortex seems to be stronger for values of negative offset.

Extensive measurement of the fluctuating velocity distributions immediately upstream of the wedge ($L - x/\theta_R = 8$) indicated that the character of the approach vortex was essentially invariant with offset ϵ, thereby providing essentially identical vortex structure for all cases (Ziada 1981). Moreover, the frequency of vortices was found to be invariant with offset ϵ, agreeing with the somewhat analogous study of Hussain & Zaman (1978). This invariability in the frequency β of oscillation and amplitude of the streamwise fluctuation velocity approaching the wedge (i.e. saturation value of $\tilde{u}(\beta)_{M1}$ and $\tilde{u}(\beta)_{M2}$) is shown in figure 18, which also shows the variation of the induced force F_{rms} and the maximum r.m.s. amplitude $(\tilde{u}(\beta)_{M1})_{x=0}$ of $\tilde{u}$ at separation with the wedge offset ϵ/θ_R for the same impingement length ($L/\theta_0 = 58$) as that for figure 17. It is evident that substantial variations in amplitude of the induced force arise from small changes in wedge offset of the order of magnitude of one local momentum thickness. The details of vortex–wedge interaction patterns, force and velocity measurements, and the nature of the shed vortex are given in a related article (Ziada & Rockwell 1982*a*). The point of note is that, since the approach

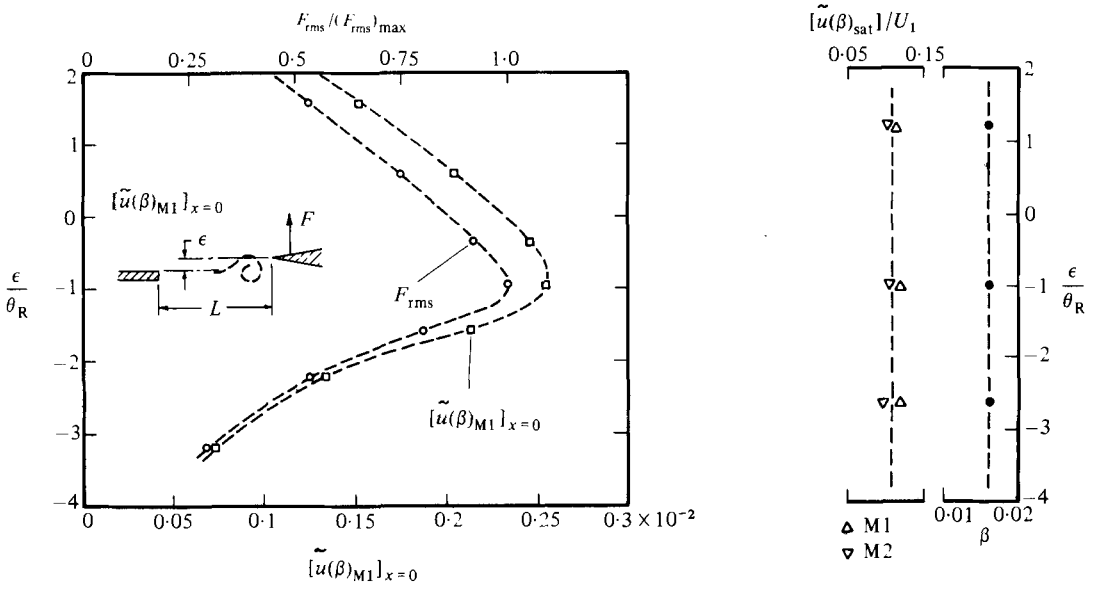

FIGURE 18. Variation of force F_{rms} and maximum fluctuation velocity $(\tilde{u}(\beta)_{M1})_{x=0}$ at separation with transverse location ϵ of wedge at constant impingement length $(L/\theta_0 = 58)$.

vortex was found to have identical characteristics for the range of ϵ examined, it is the localized interaction patterns shown in figure 17, rather than variability in the nature of the approach vortex, that result in these large variations in amplitude of the induced force.

It should be noted that, as shown in figure 18, the variation of the induced velocity fluctuation $(\{\tilde{u}(\beta)_{M1}\}_{x=0})$ at separation with wedge offset ϵ/θ_R follows that of the force F_{rms} variation, thereby linking together the upstream influence of local interaction at the wedge and the unsteady velocity field at separation. This upstream influence, in effect, corroborates the results depicted in figure 16.

Based on these observations, it can be expected that, as the impingement length L is varied at a constant value of *geometrical* offset, any flow mechanism that induces a small offset of the vortex relative to the wedge will yield a substantial change in the induced force. That is, for the case of variable impingement length L, but constant geometric offset ϵ, a 'self-induced', or 'vortex-induced' offset may result. This 'offset' can be expected to be influenced by two parameters, namely the dimensionless circulation of the vortex and its initial position well upstream of the wedge. Rogler's (1974) model is relevant in demonstrating the influence of these parameters. He considers the trajectory of a point vortex in a uniform stream past the leading edge of a semi-infinite plate. Based on his results, a very small change in the vortex strength (dimensionless circulation) and/or its initial position results in a significant change in the 'offset' between the incident vortex and the leading edge of the plate. Although the vorticity in the laboratory vortex is highly distributed, the qualitative features of its trajectory upstream of the edge should be describable via this point-vortex theory of Rogler (1974). These aspects are discussed in further detail by Ziada (1981).

In conjunction with the visualization that follows, it is appropriate to examine the magnitude of a characteristic unsteady velocity as the wedge is approached. The previously defined peak amplitude $\tilde{u}(\beta)_{M1}$ (see figure 9) is appropriate in characterizing

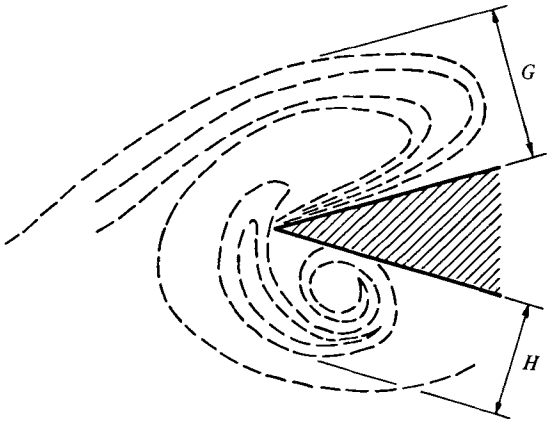

FIGURE 19. Definition of parameter γ for characterizing vortex–wedge interaction.

the strength of the core region of the vortex as a function of streamwise distance upstream of the wedge (Ziada & Rockwell 1982*a*). As shown in figure 18, the fluctuation amplitude is essentially constant (flat) for a considerable distance upstream of the wedge; furthermore, the streamwise extent of this region of constant amplitude (i.e. extent of constant strength of the incident vortex) increases as impingement length increases. This means that the length upstream of the leading edge at which a vortex of given strength 'appears' increases with increasing impingement length; according to Rogler's analysis, the vortex trajectory will be altered accordingly. Consequently, in the laboratory, a different 'offset' of the incident vortex can be expected to occur as the impingement length is changed. As noted earlier, this feature can be observed by comparing the photos (*b*), (*c*), and (*d*) of figure 6.

In characterizing the degree of 'self-induced offset' and its consequences for vortex–edge interaction as the impingement length is varied, it is helpful to use a parameter γ defined schematically in figure 19. It should be noted that characterization of vortices from flow-visualization pictures is neither the object of defining the parameter γ, nor of the present work. Clearly, the dashed lines of figure 19 do not necessarily bear any relationship to vorticity contours. However, the parameter γ permits qualitative comparisons, at a specific instant of time, between vortex–edge interaction pattern and that pattern (i.e. reference pattern) which produces the maximum force amplitude. This reference pattern is shown in photo *R* ($\epsilon/\theta_R = -1{\cdot}0$) of figure 17, and corresponds to the maximum amplitude of induced force (figure 18). By comparing photos *Q* and *S* with photo *R* (figure 17), it can be seen that as the parameter γ shifts away from unity, in either direction, the force amplitude falls. Therefore smaller offsets of the vortex relative to the leading edge or, equivalently, γ-values closer to unity result in larger amplitudes of induced force.

In the flow-visualization pictures of figure 20, each impingement length is represented by two photos: the first photo is taken when the force is at a maximum negative value; and the second photo when the force has zero value. Series (*a*) and (*b*) of figure 20 represent the vortex–wedge interaction patterns for the same impingement length ($L/\theta_0 = 44$), corresponding to the location of a frequency (and a force-amplitude) jump between stages I and II. After the system oscillated for a

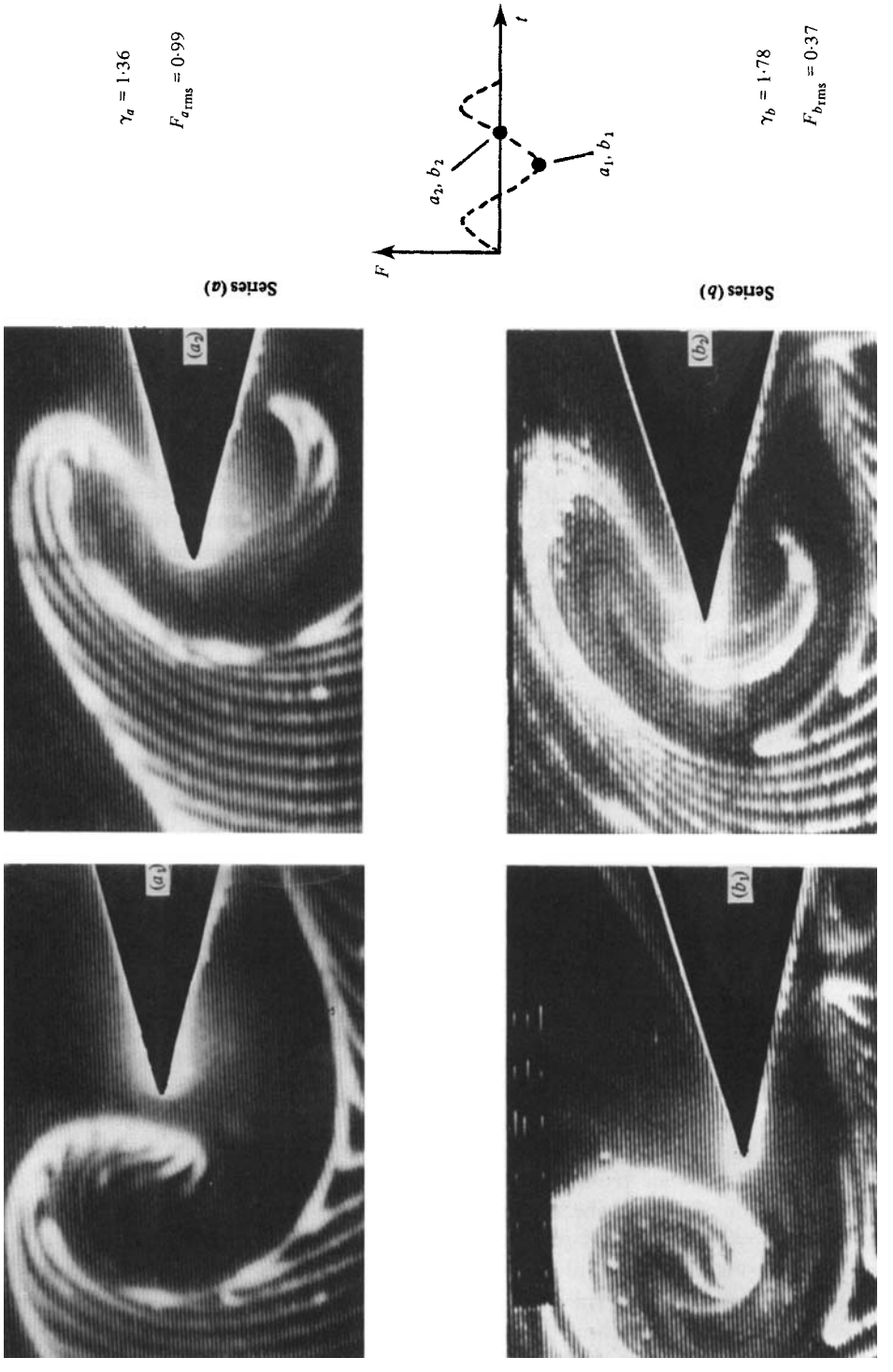
Series (a)
Series (b)
$\gamma_a = 1{\cdot}36$
$F_{a_{\rm rms}} = 0{\cdot}99$
$\gamma_b = 1{\cdot}78$
$F_{b_{\rm rms}} = 0{\cdot}37$
a_2, b_2
a_1, b_1
F
t
(a_2)
(b_2)
(a_1)
(b_1)

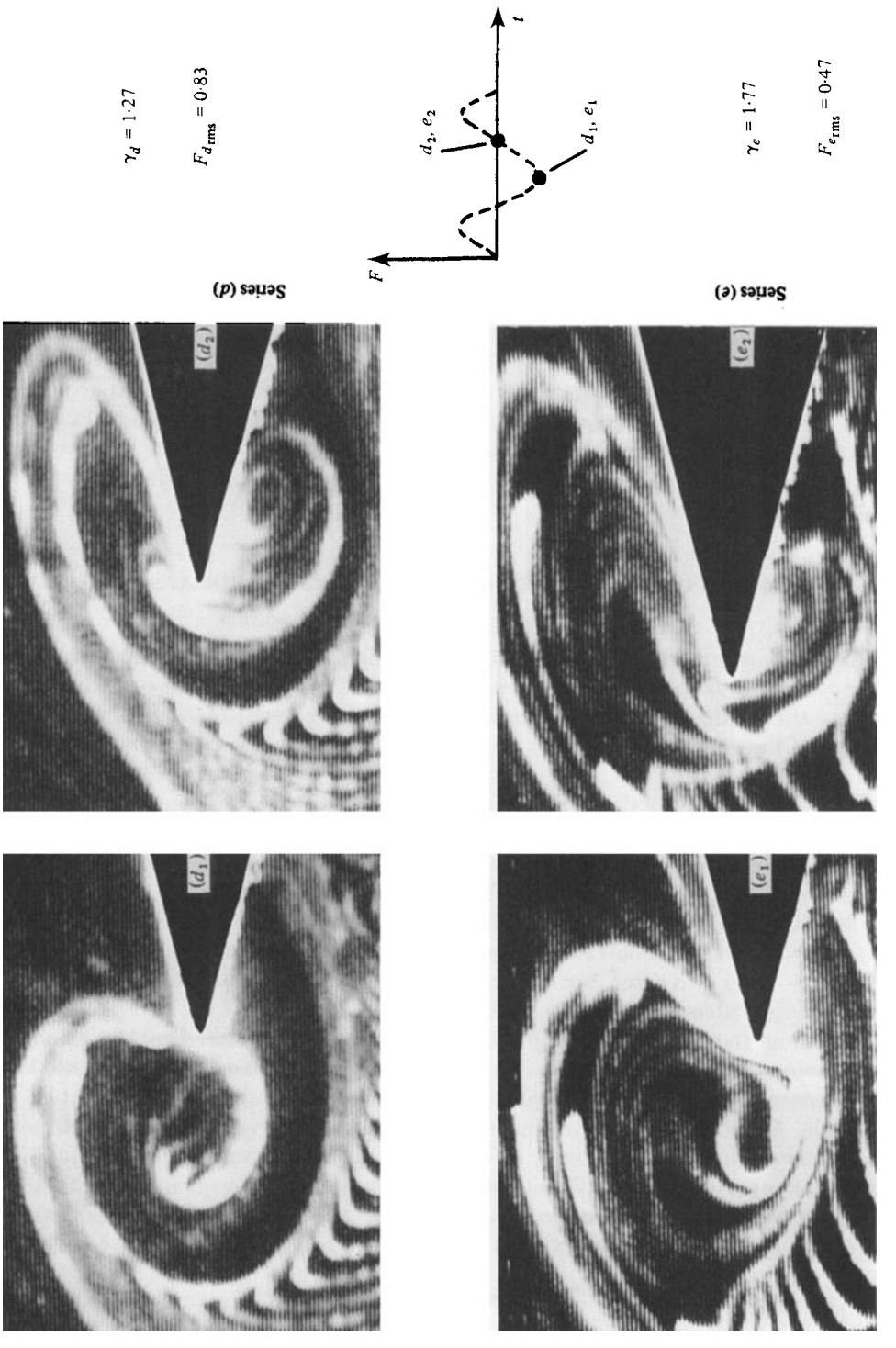

FIGURE 20. Visualization of vortex–wedge interaction patterns showing the effect of impingement length on the self-, vortex-induced transverse offset between the centre of the incident vortex and the tip of the wedge.

period in stage I, the flow was given a large perturbation and, after settling down to stationary conditions, oscillated in stage II. Series (*a*) of figure 20 depicts stage I operation corresponding to case (*a*) in figure 16, whereas series (*b*) portrays stage II operation corresponding to case (*b*) in figure 16. By close inspection of these two series, one can deduce that the vortex centre in case (*b*) is displaced above the wedge tip a larger distance than that for series (*a*) yielding $\gamma_a = 1{\cdot}36$ and $\gamma_b = 1{\cdot}78$. Thus, on the basis of the discussion in conjunction with figures 17–19, the induced force in case (*a*) must be larger than that induced in case (*b*). That this is so is evidenced in figure 16. By similar reasoning, the sudden decrease in force amplitude between stages II and III can be explained. The impingement length for case (*d*), shown in figure 16, is $L/\theta_0 = 62$ (stage II) just before the jump, and that for case (*e*) is $L/\theta_0 = 65$ (stage III) just after the jump; the corresponding vortex–edge interaction patterns are series (*d*) and (*e*) of figure 20. The parameter γ_d (= 1·27) is smaller than γ_e (= 1·77), indicating that the force in case (*d*) is larger that that in case (*e*). This agrees with the measurements shown in figure 16. Relative values of γ of $\gamma_b = 1{\cdot}78$ and $\gamma_d = 1{\cdot}27$ are likewise consistent with the relative amplitudes of the force in comparing cases (*b*) and (*d*) of figure 16. Moreover, the longer impingement length (case (*d*)) produces a lower 'offset' of the transverse vortex position ($\gamma_d = 1{\cdot}27$) than the shorter length (case (*b*); $\gamma_b = 1{\cdot}78$), agreeing with the aforementioned trend predicted by Rogler (1974).

7. Comparison of overall oscillation characteristics with linear stability theory

7.1. *Exponential growth rate of disturbances*

The disturbance growth rates, the variable levels of initial disturbance amplitude, and the streamwise phase distributions of figures 15 and 16 can be considered with regard to their influence on the overall oscillation characteristics, and compared with concepts of linear stability theory, as well as with externally excited *non*-impinging flows.

The measured rates of disturbance amplification for the aforementioned cases (*b*), (*c*) and (*d*) are compared in figure 16 with the predicted rates, using Michalke's (1965) linear spatial theory. The dimensionless frequencies for the three cases approximate the frequency $\beta_{\max}$ at which the shear layer is most unstable ($\beta_{\max} = 0{\cdot}0167$, $\beta_b = 0{\cdot}0172$, $\beta_c = 0{\cdot}016$ and $\beta_d = 0{\cdot}015$). Figure 16 shows good agreement between the measured and the theoretical rates. The agreement for case (*d*) is not as good as that for the other two cases, but the experimental data do show a lower growth rate, which is compatible with the linear-theory prediction.

Concerning the saturation amplitude of $\tilde{u}(\beta)_{\mathrm{M1}}$ shown in figure 16, Freymuth (1966), using an externally excited non-impinging jet, has demonstrated that, for constant excitation frequency, the initial amplitude has no influence on the saturation amplitude. As shown in figure 18, the initial amplitude $\{\tilde{u}(\beta)_{\mathrm{M1}}\}_{x=0}$ is a strong function of ϵ. However, both the frequency of oscillation and the saturation amplitude were found to be invariant with ϵ. So, in essence, for the constant frequency of self-excited oscillation, the saturation amplitude of $\tilde{u}(\beta)_{\mathrm{M1}}$ is independent of its initial value at separation, agreeing with the external-excitation study of Freymuth.

7.2. *Frequency of oscillation*

The phase data, shown in figure 15, illustrate the linear variation of the fluctuating velocity phase in the streamwise direction. This linear variation persists along the entire length of impingement from $x = 0$ to $x = L$ for all impingement lengths examined herein. Consequently, for each impingement length, velocity fluctuations

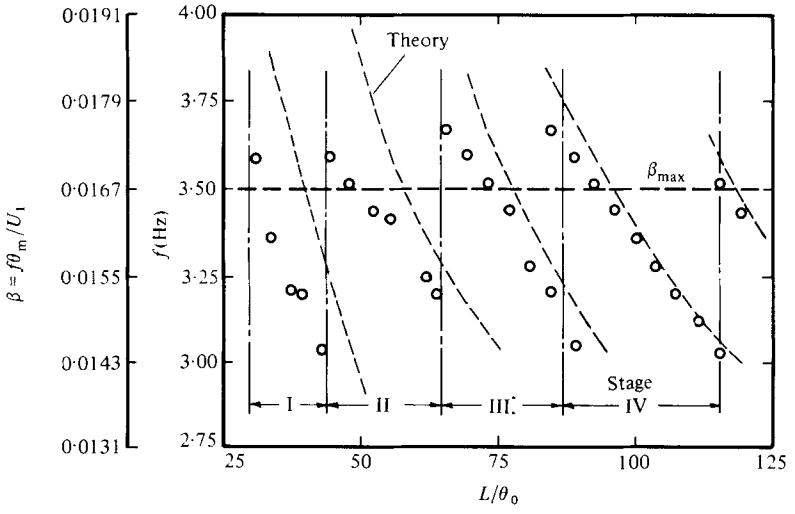

FIGURE 21. Frequency β of mixing-layer–wedge oscillation as a function of impingement length L.

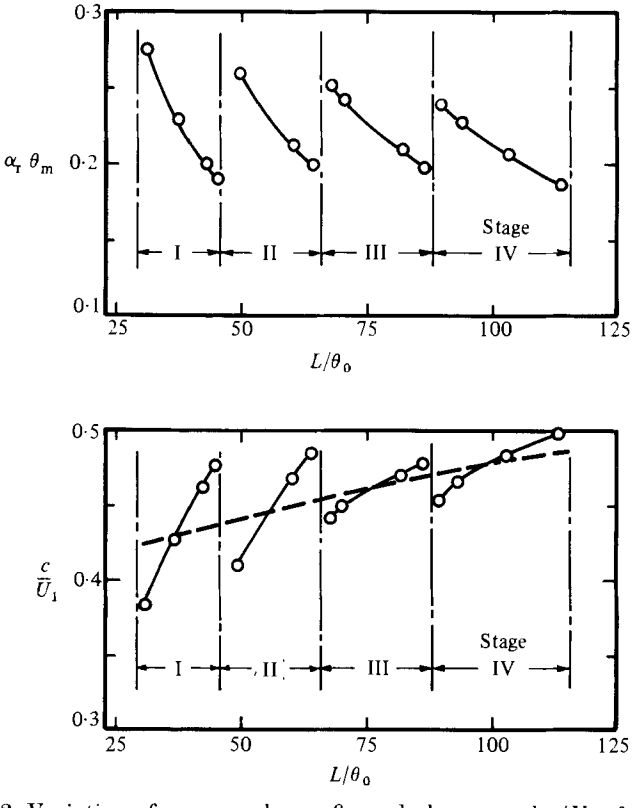

FIGURE 22. Variation of wavenumber $\alpha_r\theta_m$ and phase speed c/U_1 of the instability wave with the impingement length L/θ_0.

(of constant wavelength) convect downstream at a constant speed. Comparisons with the linear theory show good agreement with the experimentally determined growth rates (see figure 17) in the near field of separation. This indicates the dominant role of the separated shear layer at the high-speed side. Its instability characteristics determine not only the frequency of oscillation, but also the phase speed and wavelength, which are virtually constant along the entire distance from separation to impingement. Further comparison with the linear stability theory is obviously suggested to test its usefulness in predicting the frequency of oscillation.

At each impingement length, the wavelength λ and hence the wavenumber ($\alpha_r = 2\pi\theta_m/\lambda$) can be determined from the criterion $L/\lambda = n$. Corresponding to that wavenumber, the linear stability theory provides an average phase speed c. An estimate of the oscillation frequency can then be obtained from the formula $f = c/\lambda$. Figure 21 compares these predicted frequencies with the experimental results of figure 4(*a*). The agreement for the first two stages is not as satisfactory as that for the other stages of operation. However, the maximum deviation between theory and experiment is 14 %, and occurs at the beginning of stages I and II. Based on this comparison, one can conclude that the linear theory, if incorporated with a proper streamwise phase criterion, can predict the frequency of oscillation within an accuracy range of ± 15 %. No greater degree of accuracy can be expected from such a simplified model, given the crudity of the assumption concerning the characteristic length θ_m and the complexity of the flow field.

Figure 22 illustrates the dependence of the wavenumber and the phase speed on the impingement length. During each stage of operation the wavelength and the phase speed increase continuously when the impingement length is increased. In agreement with Hussain & Zaman's (1978) data, but in contrast with Sarohia's (1977) findings, the stages of operation are separated by well-defined jumps in both the wavelength and the phase speed. However, the gross trend of the phase speed variations (shown in figure 22 by the dashed line) agrees with that reported by Sarohia. He found the phase speed to increase steadily with an increase in the cavity length, without any discontinuity as the cavity switched modes of oscillation.

8. Summary and concluding remarks

The impingement of an unstable laminar mixing layer on a solid edge leads to self-generation of strongly coherent organized oscillations. Immediately downstream of separation (at the trailing edge of the splitter plate), the mean-velocity profile resembles an asymmetric wake flow. The instability associated with the low-speed side is of considerably lower frequency and has a smaller growth rate than that associated with the high-speed side. Therefore the instability characteristics of the upper shear layer (i.e. at the high-speed side) dominate, determining the frequency, wavelength and phase speed of the system oscillation. This aspect is substantiated by the good agreement between the experimental growth rates and the linear spatial stability theory in the near field of separation, and by the non-existence of any instabilities associated with the lower shear layer. Non-impinging, artificially excited asymmetric wakes can be expected to exhibit similar characteristics. Obviously, these characteristics depend on two parameters: namely the thickness of the blunt trailing edge and the ratios of momentum thickness and free-stream velocity on either side of the wake.

Phase measurements within and along the edges of the mixing layer demonstrate a number of possible interpetations of streamwise phase distributions and phase differences between separation and impingement. Only phase distributions along the

upper and the lower edges of the mixing layer seem to have an obvious significance. They vary linearly in the streamwise direction, provide the same phase difference between separation and impingement, and yield a universal phase criterion. For a self-sustained oscillation, the phase shift between velocity fluctuations at separation and impingement is found to be about $2n\pi$, where n is the stage number. In other words, the disturbance wavelength λ and the impingement length L maintain an integral relation $L/\lambda = n$ for the whole range of the impingement lengths examined. Moreover, the phase speed at which the disturbance travels in the shear layer, deduced from these streamwise phase variations, exhibits discontinuous jumps as the system switches modes (or stages).

In spite of the large transverse variations in the phase of fluctuating velocity, the overall phase across the shear layer at any streamwise station reduces to approximately π. This transverse phase criterion is found to persist along the entire length of impingement. At the trailing (separation) edge, the upstream imprint of the self-sustained oscillation is manifested in a π phase difference at edges of the upper and lower shear layers, and extending into the free stream. Furthermore, corresponding locations in the upper and lower shear layers are also approximately π out of phase. This compatibility between the downstream dynamics and the character of the trailing-edge unsteadiness may have significant consequences for non-impinging shear layers as well.

Prediction of the frequency of system oscillation (within $\pm 15\,\%$ accuracy limits) can be achieved with the aid of the linear stability theory if incorporated with a proper streamwise phase criterion for sustained oscillations. The use of the linear theory of parallel flow to provide an average value of phase speed is justified by the linear variations of the streamwise phase distributions measured at the edges of the shear layer, indicating that the wavelength (and consequently the phase speed) is constant along the entire length of impingement.

The velocity-fluctuation amplitude at separation is approximately proportional to the force induced at the edge. If the induced velocity fluctuation at the trailing (separation) edge varies in amplitude while the oscillation frequency is held constant, the equilibrium level of fluctuation in the downstream (nonlinear) region of the shear layer takes on essentially identical values. This, in agreement with previous investigations of artificially excited, non-impinging jet flows, implies that the 'strength' of a self-sustained oscillation must be carefully specified in terms of either the saturation level of velocity fluctuations *or* the magnitude of the induced force at a given oscillation frequency.

The fact that the induced force at the edge takes on substantially different values for essentially identical fluctuation level of the approach flow is associated with the varying nature of the vortex–edge interaction mechanism. Small 'offsets' of the incident vortex, relative to the edge, of only one momentum thickness considerably alter the amplitude of the induced force. In effect, there are two means of producing vortex 'offset'. The first involves transverse variation of the edge location at a constant value of impingement length. The second means might be termed a 'self-induced offset', arising in cases where the transverse location of the edge in the mixing layer is held constant while the impingement length is varied; since the streamwise extent of the nonlinear saturation region increases as the impingement length increases, the essential consequence is alteration of the relative location upstream of the edge at which vortices are 'formed'. This is equivalent to changing the initial position (i.e. point of 'appearance') of the incident vortex with respect to the impingement edge. Vortices with different 'initial positions' approach the edge along slightly different trajectories. The result is a small alteration of the transverse

offset of the incident vortex, which in turn substantially alters the magnitude of the induced force.

The well-known occurrence of frequency jumps as the impingement lengthscale is varied is shown to be associated with substantial jumps in amplitude of the force induced on the wedge. In turn, these abrupt alterations in force amplitude are related to the aforementioned vortex–edge interaction mechanisms.

The authors wish to thank Professor M. V. Morkovin for his comments on the experimental results. Financial support was provided by the National Science Foundation of Washington, D.C., and the Volkswagen Foundation of Hannover, West Germany.

REFERENCES

Brown, G. B. 1937 The vortex motion causing edge tones. *Proc. Phys. Soc.* **49**, 493–507.

Ffowcs Williams, J. E. 1969 Hydrodynamic noise. *Ann. Rev. Fluid Mech.* **1**, 197–222.

Freymuth, P. 1966 On transition in a separated laminar boundary layer. *J. Fluid Mech.* **25**, 683–704.

Hill, P. G. & Stenning, A. H. 1960 Laminar boundary layers in oscillatory flow. *Trans. A.S.M.E.* D: *J. Basic Engng* **82**, 593–608.

Ho, C. & Nosseir, N. S. 1981 Dynamics of an impinging jet. Part 1. The feedback phenomenon. *J. Fluid Mech.* **105**, 119–142.

Hussain, A. K. M. F. & Zaman, K. B. M. Q. 1978 The free shear layer tone phenomenon and probe interference. *J. Fluid Mech.* **87**, 349–383.

Karamcheti, K., Bauer, A. B., Shields, W. C., Stegen, G. R. & Woolley, J. A. 1969 Some basic features of an edgetone flow field. *Basic Aerodynamic Noise Research: Conf. at NASA Headquarters, Wash. D.C.*, 14–15 *July. NASA-SP*-207, p. 275.

Knisely, C. & Rockwell, D. 1982 Self-sustained low-frequency components in an impinging shear layer. *J. Fluid Mech.* **116**, 157–186.

McCartney, M. S. & Greber, I. 1973 An experimental and theoretical investigation of the edge-tone phenomenon. *Case Western Reserve University Rep.* FTAS/TR73-87.

Michalke, A. 1965 On spatially growing disturbances in an inviscid shear layer. *J. Fluid Mech.* **23**, 521–544.

Miksad, R. W. 1972 Experiments on the nonlinear stages of free-shear transition. *J. Fluid Mech.* **56**, 695–719.

Powell, A. 1961 On the edgetone. *J. Acoust. Soc. Am.* **33**, 395–409.

Richardson, E. G. 1931 Edge-tones. *Proc. Phys. Soc.* **43**, 394–404.

Rockwell, D. & Naudascher, E. 1979 Self-sustained oscillations of impinging free shear layers. *Ann. Rev. Fluid Mech.* **11**, 67–94.

Rockwell, D. & Schachenmann, A. 1982 Self-generation of organized waves in an impinging turbulent jet at low Mach number. *J. Fluid Mech.* **117**, 425–441.

Rogler, H. L. 1974 A mechanism of vorticity segregation. *Bull. Am. Phys. Soc. Ser. II* **19**, 1165.

Sarohia, V. 1977 Experimental investigation of oscillations in flows over shallow cavities. *A.I.A.A. J.* **15**, 984–991.

Stuart, J. T. 1967 On finite amplitude oscillations in laminar mixing layers. *J. Fluid Mech.* **29**, 417–440.

Ziada, S. 1981 Self-sustained oscillations of a mixing layer–wedge system. Ph.D. thesis, Dept of Mech. Engng and Mechanics, Lehigh University.

Ziada, S. & Rockwell, D. 1981*a* Vortex–leading-edge interaction. *J. Fluid Mech.* **118**, 79–107.

Ziada, S. & Rockwell, D. 1982*b* Generation of higher harmonics in an unstable mixing layer–edge system. *A.I.A.A. J.* **20**, 196–202.